Agricultural and Forest Meteorology 385 (2026) 111219

Contents lists available at ScienceDirect

Agricultural and Forest Meteorology

journal homepage: www.elsevier.com/locate/agrformet

Critical soil moisture thresholds for evapotranspiration in rainfed semi-arid maize in Kenya

Matti Räsänen [a,*], Julius Omondi [b,d], Vincent Odongo [c], Temesgen Abera [d,i], Juuso Tuure [e], Janne Heiskanen [d,h], Cheng-I Hsieh [f], Laura Alakukku [e], Lutz Merbold [g], Petri Pellikka [d,j,k], Timo Vesala [b,l]

[a] Department of Forest Sciences, University of Helsinki, Finland
[b] Institute for Atmospheric and Earth System Research/Physics, University of Helsinki, Finland
[c] International Livestock Research Institute, Kenya
[d] Department of Geosciences and Geography, University of Helsinki, Finland
[e] Department of Agricultural Sciences, University of Helsinki, Finland
[f] Department of Bioenvironmental Systems Engineering, National Taiwan University, Taiwan
[g] Research Division Agroecology and Environment, Agroscope, Switzerland
[h] Finnish Meteorological Institute, Finland
[i] University of Marburg, Germany
[j] Finnish Southern Africa Cooperation Institute, 10 Schwabe Street, Windhoek, Namibia
[k] Department of Geography, University of Cambridge, Cambridge, United Kingdom
[l] Institute for Atmospheric and Earth System Research/Forest Sciences, University of Helsinki, Finland

ARTICLE INFO

Keywords:
Maize growth stages
Soil moisture content
Soil matric potential
SEBS
ERA5

ABSTRACT

Understanding how maize (*Zea mays* L.) evapotranspiration (ET) and its drivers vary under rainfed semi-arid conditions remains limited, despite general estimates across growth stages. This study aimed to quantify growth stage–specific ET in rainfed maize, characterize its soil and atmospheric controls, and evaluate seasonal and interannual variability using the Surface Energy Balance System (SEBS) model. ET was measured using the eddy covariance method over two long rainy seasons. Crop growth stages were identified using the normalized difference vegetation index (NDVI) from Sentinel-2, and ERA5 reanalysis data were used as inputs for the SEBS model. The measured growing-season ET ranged from 221 to 269 mm season^{-1} for the two wet years. However, long-term SEBS estimates (2014–2022) revealed rainfall control on soil moisture and ET, with seasonal ET spanning 94–408 mm season^{-1}. Results show that the critical soil moisture threshold (θ_{crit}) separating non-stressed and water-stressed ET conditions is not a fixed soil property but varies with crop growth stage and soil depth. Growth-stage-specific θ_{crit} at 0.1 m depth ranged from 0.05 to 0.07, while growing-season θ_{crit} derived from ET_{SEBS} varied from 0.04 to 0.09 across years. The ET–soil matric potential relationship exhibited stage-specific hydraulic thresholds (–1.5 MPa during early vegetative and –1.3 MPa during reproductive stages), reflecting shifts in soil–plant hydraulic functioning across the season. Together, these stage-specific moisture and stress thresholds clarify ET responses to soil and rainfall dynamics, enhancing crop-model parameterization and informing water-management strategies in rainfed semi-arid maize systems.

1. Introduction

Evapotranspiration (ET)—the combined process of water loss via soil evaporation and plant transpiration—is a fundamental component of the terrestrial water cycle and plays a pivotal role in food production, including in crops such as maize (Allen et al., 1998). In semi-arid regions, ET responses are particularly sensitive to soil moisture availability and atmospheric demand, as erratic rainfall and rapid drying strongly influence crop water use and performance. A deeper understanding of the soil moisture–plant–atmosphere interactions governing ET is therefore essential for improving water management and sustainability in rainfed semi-arid maize systems.

Rainfed maize production in semi-arid areas operates under

* Corresponding author.
E-mail address: matti.rasanen@helsinki.fi (M. Räsänen).

https://doi.org/10.1016/j.agrformet.2026.111219
Received 22 September 2025; Received in revised form 8 April 2026; Accepted 29 April 2026
Available online 5 May 2026

List of symbols and abbreviations used in the manuscript

Abbreviations

BBCH	Biologische Bundesanstalt, Bundessortenamt und CHemische Industrie
ERA5	the fifth generation of the European Centre for Medium-Range Weather Forecasts (ECMWF) Reanalysis dataset.
ET	evapotranspiration measured by eddy covariance
ET_{SEBS}	Evapotranspiration estimated using the SEBS model.
LST	Land Surface Temperature
MODIS	Moderate Resolution Imaging Spectroradiometer
NDVI	Normalized Difference Vegetation Index
P	Growing season rainfall.
PM	Penman-Monteith
SEBAL	Surface Energy Balance Algorithm for Land
SEBS	Surface Energy Balance System model
SMC	Soil Moisture Content
SMC_{end}	Soil moisture content at the end of the growing season.
SMC_{init}	Initial surface soil moisture content at the start of the growing season.
SMP	Soil Matric Potential
TSEB	Two-Source Energy Balance model
VPD	Vapor Pressure Deficit
WUE	Water-Use Efficiency

Symbols

β	Bowen ratio
C_p	Specific heat capacity of air
G_a	Aerodynamic conductance
G_s	Surface (stomatal) conductance
LW_d	Downward longwave radiation
LW_u	Upward longwave radiation
Ψ	Soil matric potential
Ψ_{crit}	Critical soil matric potential threshold linked to ETcrit
R_n	Net radiation
ρ	Air density
SW_d	Downward shortwave radiation
SW_u	Upward shortwave radiation
θ_{crit}	Critical soil moisture content (the soil moisture threshold at which ET becomes soil moisture limited, i.e., onset of plant water stress)
u	Wind speed above the canopy
u*	Friction velocity
Δ	Slope of the saturation vapor pressure curve
γ	Psychrometric constant

fundamentally different biophysical constraints than in the high-yield maize systems. Early-maturing maize varieties, sparse planting densities, and incomplete canopy closure result in prolonged soil exposure and a relatively large contribution of soil evaporation to total ET. In the present study area, Southeastern Kenya, climate follows a bimodal rainfall pattern, with long rains (March–May) and short rains (October–December), though their timing and duration vary spatially (Leclerc et al., 2014; Mwalusepo et al., 2015; Nicholson, 2017). The onset of the long rains is critical for maize establishment, yet rainfall trends since 2005 indicate increasing deficits and more frequent droughts (Nicholson, 2017). Even in years with similar total rainfall, variations in timing, frequency, and intra-seasonal distribution complicate moisture management and crop productivity (Leclerc et al., 2014; Mwalusepo et al., 2015). Smallholder farmers, who rely entirely on rainfall for subsistence, are especially vulnerable to shifts in rainfall patterns that threaten germination, growth, and subsequently yields (Salami et al., 2010).

To mitigate moisture losses, farmers employ adaptive land management strategies such as contouring, pre-planting weed removal, and adjustments in planting density (Marimi, 1979; Shilomboleni et al., 2024). In Kenya, these approaches are complemented using fast-maturing hybrid maize varieties that align with the rainfall seasons. While these practices reduce the risk of total crop failure, increasing climate variability has heightened the need for a process-based understanding of how soil water availability regulates evapotranspiration (ET) under rainfed conditions.

A critical limitation in advancing ET understanding in rainfed systems is the scarcity of direct, continuous field measurements. Soil moisture content and soil matric potential (Ψ) are primary controls on ET, yet their interactions across soil depths and crop developmental stages remain insufficiently quantified in the context of rainfed maize. Although previous studies have demonstrated that soil moisture availability strongly influences maize ET (Krell et al., 2021), the soil moisture thresholds beyond which ET declines due to crop water stress remain poorly constrained. It is unclear whether such thresholds vary across maize growth stages or shift between seasons characterized by crop failure and favorable yields. Conceptual ecohydrological and crop water balance frameworks commonly represent the onset of water stress using a single, time-invariant soil moisture threshold (e.g., s*), which assumes an average plant hydraulic response over the growing season (Vico and Porporato, 2011). While recent rainfed maize studies have improved process representation by explicitly separating soil evaporation and transpiration responses to soil moisture (e.g., Krell et al., 2021), stress thresholds in these approaches are prescribed parameters, and their potential variability across crop development or between seasons is not explicitly evaluated.

Several models exist for ET estimation, ranging from empirical to energy balance-based approaches. The Penman-Monteith (PM) equation, widely used in ET studies, achieves high accuracy when adequately parameterized (Allen et al., 1998; García-Gutiérrez et al., 2021). However, its reliance on extensive in situ measurements—including canopy structure, soil properties, and meteorological data—limits its applicability in smallholder farms caused by a paucity of data. Energy balance–based models—such as the Surface Energy Balance Algorithm for Land (SEBAL; Bastiaanssen et al., 1998), the Two-Source Energy Balance (TSEB) model (Norman et al., 1995), and the Surface Energy Balance System (SEBS; Su, 2002)—estimate evapotranspiration (ET) by integrating remotely sensed land surface temperature (LST) with meteorological inputs. However, even advanced all-weather LST products can be biased in African environments, often due to thin surface moisture films from dew or light rainfall that insulate the land–atmosphere interface but are difficult to detect remotely (Dowling et al., 2022). Among these, SEBS has been widely applied due to its adaptability in heterogeneous landscapes and semi–arid environments with fluctuating water availability (Chen and Liu, 2020; Pervez et al., 2021; Wanniarachchi and Sarukkalige, 2022). While SEBS-derived ET estimates have shown reasonable agreement with ground-based measurements (Xue et al., 2020), discrepancies remain due to uncertainties in input data and model assumptions. Additionally, while studies have evaluated SEBS performance in semi-arid and temperate climates (Acharya and Sharma, 2021), its reliability in semi-arid tropical maize-growing regions remains unclear and understudied, necessitating validation against field measurements.

The performance of SEBS depends on the quality of its meteorological inputs and surface temperature estimates, which can be biased under conditions of sparse vegetation and variable soil moisture conditions common in semi-arid regions. These uncertainties highlight the need for careful evaluation of SEBS-derived ET against field observations. To address these challenges, this study applies SEBS in combination with ERA5 reanalysis data to assess long-term ET dynamics in a semi-arid maize system. Studies have demonstrated that ERA5 effectively supplements ground-based measurements to model ET using SEBS (Huang and Huang, 2023). Despite some biases—such as overestimated shortwave radiation and underrepresented cloud effects—ERA5 provides high-resolution meteorological inputs, including net radiation and wind speed, which improve ET estimates across diverse landscapes (Elkatoury et al., 2024).

To address these knowledge gaps, this study explicitly tests whether critical soil moisture and matric potential thresholds governing ET in rainfed maize are fixed properties or dynamic features that vary with crop development, soil depth, and interannual rainfall conditions. Using a combination of direct eddy covariance measurements and multi-year model ET estimates, we investigate how ET sensitivity to soil moisture evolves within and across growing seasons in a semi-arid rainfed system. Specifically, this study aims to: (1) quantify daily and growth-stage-specific variability in maize ET using two years of direct eddy covariance observations; (2) characterize the relationships between ET, soil moisture content, soil matric potential, and surface conductance–vapor pressure deficit across maize growth stages; and (3) assess seasonal and interannual variability in ET–soil moisture relationships using SEBS model estimates for maize growing seasons from 2014 to 2022.

2. Methodology

2.1. Site description

The measurements were conducted on a smallholder farm in Maktau, Taita Taveta County, Kenya (3° 25′33 S, 38° 8′22 E, 1060 m a.s.l, Fig. 1) during the long rainy seasons in 2019 and 2020. Soil at the field site is *Ferralsol* (Wachiye et al., 2020) having a texture of sandy clay loam with a 0.74 sand and a 0.22 clay fraction (Räsänen et al., 2020). The soil fertility is poor and lacking organic material. During both long rainy seasons, the same hybrid maize seed was sown. The maize seed originated from Kenya seed company (variant DH02). The seeds are fast growing, tolerant to water stress (intended for areas with 200–500 mm of annual rainfall), and commonly grown by farmers in this region. It is expected to mature within 70 to 100 days after sowing. Typically, the long rains season begins in March, with farmers waiting for the first rainfall to plant maize. In 2019, delayed rains, absent in March, led to planting on April 12 after a 24 mm rainfall event in the second week of April. In contrast, 2020 saw timely rains in the second week of March, allowing planting in the third week of March. The maize was harvested 123 and 135 days later on August 13, 2019, and July 30, 2020, respectively. Most of the maize roots were found at a soil depth of 0.2 and 0.3 m based on excavation of two mature maize plants.

2.2. Meteorological and soil measurements

The eddy covariance system (Aubinet et al., 2012) was installed at the northern end of the crop field (Fig. 1). The measurement system

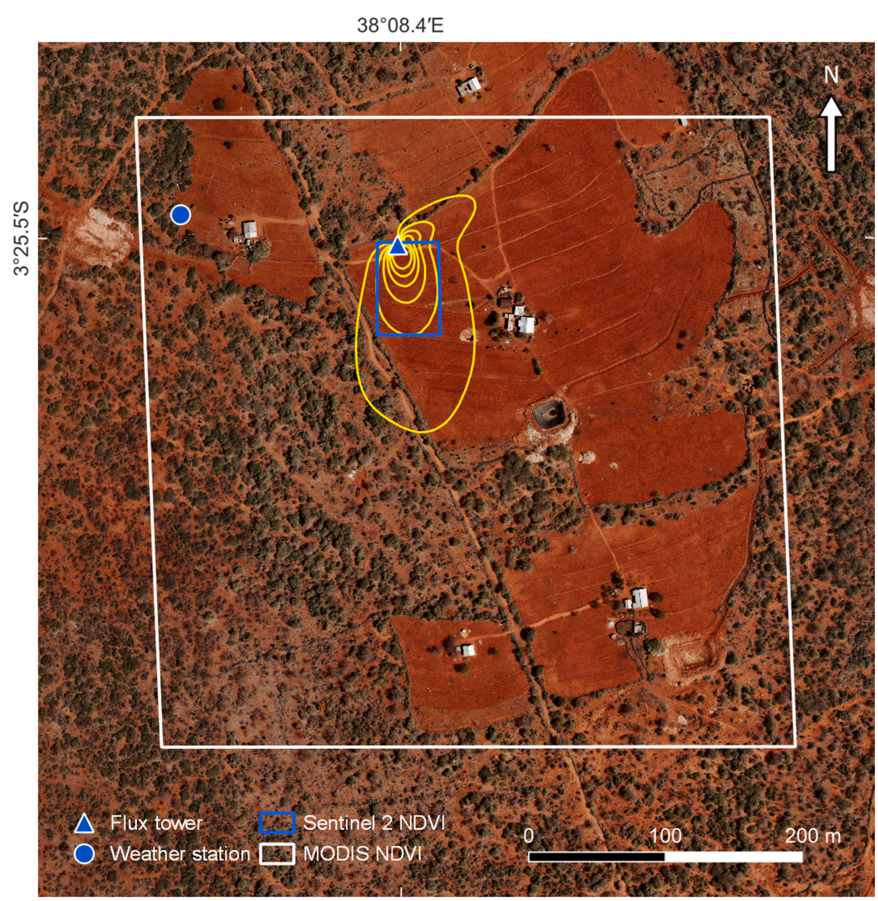

Fig. 1. Map of the field experiment setup. The blue triangle indicates the eddy covariance mast. Footprint climatology contour lines (yellow), based on combined data from the 2019 and 2020 growing seasons, are shown from 10% to 90% (Kljun et al., 2015). Blue box denotes region for extracting Sentinel NDVI and white box denotes MODIS NDVI pixel. The 80% footprint contour closely overlaps the blue Sentinel NDVI region. The maize field is the open crop field around the eddy covariance mast surrounded by savanna bushland.

consisted of a 3D sonic anemometer (Gill WindMaster Pro, Gill Instruments Ltd., Lymington, Hampshire, UK) and an open path infrared gas analyzer (LI-COR 7500DS, LI-COR Biosciences, Lincoln, NE, USA), which were positioned 3.1 m above the ground surface. The sensors were mounted to a standard scaffolding. Latent heat (LE) and sensible heat (H) fluxes were recorded every 30 min using the Licor Smartflux data logger.

Long-term meteorological measurements included wind speed and direction, rainfall, air temperature and humidity, soil moisture content, incoming solar radiation, and air pressure at 1.5 m height. The meteorological measurements cover the period from March 2014 to August 2022. The rainfall measurements at 1.5 m height were corrected for the under-catch error by multiplying them by 1.05. This factor was determined by comparing the rainfall measured at 1.5 m with a pit gauge measurement that measured rainfall at ground level (Fig. S1). Soil moisture content and soil temperature were recorded at 0.1, 0.3, and 0.5 m depth using Campbell CS650 sensors that were calibrated for the soil. The soil matric potential (Ψ) was measured at 0.1, 0.3, and 0.5 m depth using ceramic senssors (MPS-6, Decagon Devices Inc.). The fenced area for meteorological measurements was located 150 m east of the eddy-covariance mast. The net radiation measurements were placed at 4 m height and 2 m away from the eddy covariance station fencing. The four-component net radiation sensor (Hukseflux NR01) was measuring ground(surface) reflectance the first growing season in 2019. The instrument failed due to rodent damage before the start of the second growing season. The meteorological sensors made measurements every minute and using the Campbell CR3000 logger, the 30-minute averages were stored.

2.3. Flux calculation and gap-filling

The turbulent fluxes of latent and sensible heat were calculated using the EddyPro (version 7.0.9, LI-COR Biosciences, USA) software. The following processing steps were used in calculating 30-min flux averages from the raw 10 Hz data. The data were despiked (Vickers and Mahrt, 1997), detrended using block averaging and coordinate rotation was done using the double rotation. The fluxes were corrected for the effects of high and low-pass filtering (Massman, 2000; Moncrieff et al., 2004) and air density fluctuations (Webb et al., 1980). The data quality guidelines from (Mauder and Foken, 2004) were used by discarding measured flux values when the quality flag was 2. Data during rainy periods was excluded as rain has an impact on the performance of open-path analyzer. Furthermore, flux values were discarded when wind direction was $<50^\circ$ or $>200^\circ$, to restrict the fluxes to the maize field (Fig. 1). The uncorrected energy balance closure ratio in 2019, calculated as the slope of the regression between available energy and turbulent fluxes, was 0.67. The ET flux was adjusted using Energy Balance Ratio method (Volk et al., 2021). Since net radiation measurements were unavailable in 2020, the annual mean energy balance correction factor derived from 2019 was applied to the 2020 ET fluxes. The meteorological variables and the turbulent heat fluxes were gapfilled using marginal distribution sampling (MDS) from the REddyProc package (Reichstein et al., 2005). The flux footprint was estimated using a standard 2D footprint model (Kljun et al., 2015). Daytime measured variables for the two growing seasons were used to calculate the footprint climatology (Fig. 1). This footprint calculation shows 80% of the ET fluxes originate from the maize field. Soil heat flux was measured with three self-calibrating heat flux plates (Campbell HFP01SC) at 0.05 m depth. The average of the three heat flux sensors was used. The soil heat flux at 0.05 m depth was scaled to the surface level using the soil surface temperature measurements (Campbell TCAV) according to the equations in the manual.

2.4. Satellite data

Changes in maize field vegetation cover from 2014 to 2022 were quantified using daily values of the MODIS Normalized Difference Vegetation Index (NDVI) at 500 m spatial resolution from Sentinel Hub (Sinergise Solutions d.o.o., 2024). NDVI is generated from the combined MODIS Terra and Aqua Nadir Bidirectional Reflectance Distribution Function (BRDF)-Adjusted Reflectance (NBAR) product (MCD43A4 V006). MODIS NDVI was extracted for the pixel containing the flux tower (Fig. 1). In addition, higher spatial resolution Sentinel-2 NDVI was retrieved, due to its superior spatial resolution, for the eddy covariance measurement period to improve the match between the measurement footprint and satellite data. NDVI was calculated using the red (band 4) and near infrared (band 8) spectral bands at 10 m resolution from the Sentinel-2 Surface Reflectance product in Google Earth Engine. Cloud-contaminated pixels were masked using the Sentinel-2 Cloud Probability dataset. Sentinel-2 NDVI was computed for an area that covers majority of the 80% footprint of the eddy covariance measurement (Fig. 1, yellow contour overlapping blue box).

2.5. Determination of maize growth stages

To support further maize ET analysis at maize growth stage level in the present study, high-resolution Sentinel-2 NDVI data—more responsive to short-term vegetation changes—were used to delineate maize growth stages. Based on detailed analysis of Sentinel-2 NDVI trends from the 2019 and 2020 growing seasons—and in line with established phenological benchmarks (Meier, 2018; Raun et al., 2005)—we defined three distinct growth stages. The early vegetative stage: characterized by low NDVI values corresponding to initial leaf emergence and early stem elongation ($0.15 < \mathrm{NDVI} < 0.4$), the late vegetative stage: capturing the period of rapid canopy expansion ($0.4 \leq \mathrm{NDVI} \leq 0.5$), and the reproductive stage defined from NDVI > 0.5 to the point of peak NDVI through subsequent canopy decline associated with grain filling, fruit development, ripening, and senescence (Fig. 2). Days after sowing (DAS) intervals were also derived based on both literature and our observed data. See details in Table 1.

2.6. Surface conductance

Surface conductance (G_s) represents the efficiency of water vapor exchange from the soil or canopy to the atmosphere. It was calculated by inverting the Penman-Monteith equation:

$$G_s = \left(\frac{1}{G_a}\left(\frac{\Delta}{\gamma}\beta - 1\right) + \frac{\rho C_p \mathrm{VPD}}{\gamma(R_n - G)}(\beta + 1)\right)^{-1} \quad (1)$$

where G_a is the aerodynamic conductance, Δ is the slope of the saturation curve, γ is the psychrometric constant, β is the Bowen ratio, ρ is the air density, C_p is the specific heat capacity of air at constant pressure, *VPD* is the vapor pressure deficit, R_n is the net radiation, and G is the soil heat flux. The aerodynamic conductance was estimated as $\frac{u_{\mathrm{star}}^2}{u}$ where u_{star} is the friction velocity and u is the wind speed above the canopy. Daily averages of G_s were calculated by averaging the values from 10am to 2pm., the period of peak insolation and stable canopy conditions yielding representative stomatal conductance.

2.7. Investigating the ET vs SMC, ET vs SMP and Gs vs VPD relationships

To analyse the relationship between evapotranspiration (ET) and soil moisture content a two-segment piecewise linear regression was employed. The breakpoint of the fitted relationship was defined as the critical soil moisture threshold (θ_{crit}), representing the soil moisture value at which the slope of the ET–SMC relationship changed. For each growth stage and season, (θ_{crit}) was identified separately for SMC at 0.1 m and 0.3 m depths. The ET–SMP relationship was characterized using a nonlinear regression function. The critical soil matric potential (Ψ_{crit}) was obtained by mapping the ET value corresponding to θ_{crit} onto the fitted ET–SMP curve and projecting it to the SMP axis for each growth

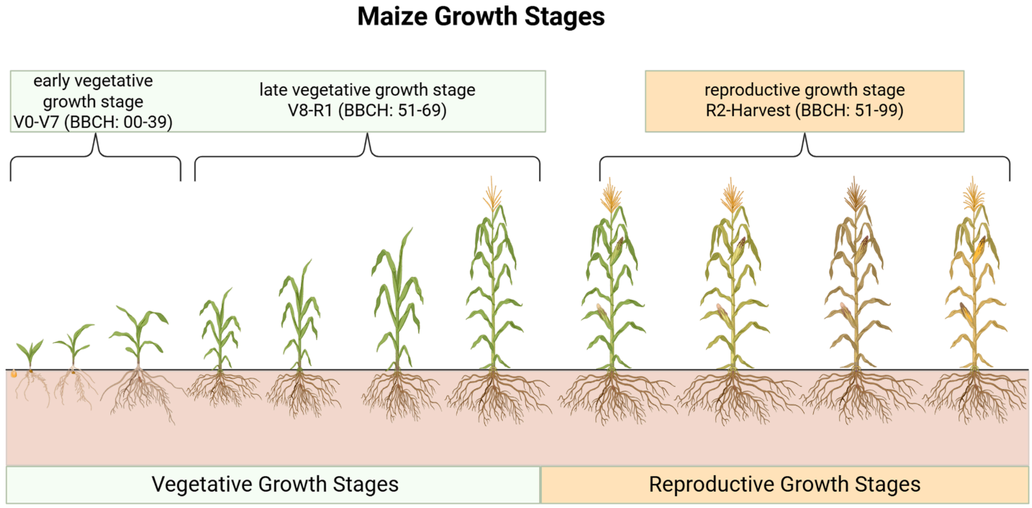

Fig. 2. Maize growth stages, where *V* denotes vegetative and *R* denotes reproductive stages (Raun et al., 2005). The BBCH scale refers to the *Biologische Bundesanstalt, Bundessortenamt und Chemische Industrie*, a standardized German system for describing plant growth stages (Meier, 2018). Created in BioRender. Omondi, J. (2025) https://BioRender.com/y6rhon2.

Table 1
Maize V–R growth stage classification methods based on Sentinel-2 NDVI: canopy development descriptions, observed vs. literature NDVI thresholds, and days after sowing (literature and 2019–2020 field data).

Growth Stage	Canopy development	NDVI Range (Observed)	NDVI Range (Literature)	DAS (Literature)	DAS (2019)	DAS (2020)
early vegetative V0-V7 (BBCH 00–39)	Initial leaf emergence, early stem elongation; sparse canopy	0.15 – 0.40	0.0 – 0.56	0–38	0–27	0–43
late vegetative V8-R1 (BBCH 51–69)	Rapid canopy expansion leading to near-complete closure	0.40 – 0.64 (2019) 0.40 – 0.55 (2020)	0.70 – 0.73	45–72	28–54	44–69
reproductive R2-Harvest (BBCH 70–99)	Canopy declines through grain filling, fruit development, ripening, and senescence.	0.64 – 0.2 (2019) 0.55 – 0.2 (2020)	0.68 – 0.17	80–129	55–123	70–135

DAS = days after sowing.

stage. Surface conductance (G_s) response to vapor pressure deficit (VPD) was characterized using power-law equations reflecting the documented exponential decline of G_s with increasing VPD (Yue et al., 2022). Parameters for each relationship were estimated through nonlinear and linear regression techniques to capture stage-specific ET and G_s behaviour under varying soil and atmospheric conditions.

2.8. SEBS estimate of daily ET

Daily ET was estimated with the SEBS model (Su, 2002) for each growing season (March 15–August 15) from 2014 to 2022. SEBS is a single-source model that estimates evaporative fraction and turbulent fluxes from radiative and meteorological input data. SEBS does not estimate separate energy balances for soil and vegetation components. The main model inputs are the four radiative components, meteorological measurements (air pressure, air temperature, relative humidity, wind speed) and the NDVI, which is used to derive on-site surface roughness parameters (Table 2). The ERA5 reanalysis data were used for the meteorological input and upward shortwave radiation (SWu) and downward longwave radiation (LWd) (Hersbach et al., 2020). The daily mean SWu and LWd were similar to the measured SWu and LWd during the growing season 2019 (Fig. 3). The downward shortwave radiation (SWd) was calculated from the linear relationship between measured locally incoming global radiation and measured incoming solar radiation (Fig. S2). The ERA5 upward longwave radiation (LWu) differed from the measured LWu (Fig. 3). The SEBS model is known to be sensitive to the LWu input (Chen et al., 2013). The SEBS model input LWu was calculated using the long-term measurements of surface soil temperature at 0.1 m depth that minimizes the difference between measured ET and ET_{SEBS}. The soil temperature at 0.1 m depth was phase-adjusted to match the surface soil temperature by applying a 3-hour lag. We then adjusted the magnitude of the surface soil moisture estimate using linear regression so that the difference between measured ET and (ET_{SEBS}) was minimized in year 2019. The surface soil temperature was converted to LWu using the Stefan-Boltzmann law with an emissivity of 0.97.

2.9. Statistical methods

Linear regression was used to quantify relationships between on-site observations, reanalysis inputs, and model-derived variables. Regression metrics included the coefficient of determination (R^2), regression slope, mean bias error, and root mean square error (RMSE), with on-site measurements treated as the reference. Similar method was used to compare measured ET and SEBS estimated ET. All statistical analyses were done using the SciPy Python package.

To identify the critical thresholds in the relationship between ET and soil moisture, piecewise linear regression was applied using the Python

Table 2
SEBS ET model input between years 2014 and 2022. Input variables used in the model: downward shortwave radiation (SWd), upward shortwave radiation (SWu), downward longwave radiation (LWd), upward longwave radiation (LWu), net radiation (Rn), soil heat flux (G), friction velocity (u_{star}), air temperature (T_a), and relative humidity (RH).

No.	Input variable	Source	Spatial resolution	Temporal resolution
1	SWd	Calculated from local incoming solar radiation	Point	30 min average
2	SWu	ERA5 reanalysis	31 km × 31 km	Hourly
3	LWd	ERA5 reanalysis	31 km × 31 km	Hourly
4	LWu	Calculated from surface soil temperature that minimizes the difference between measured ET and SEBS ET.	Point	30 min
5	R_n	Sum of radiative components	31 km × 31 km	Hourly
6	G	Calculated from Rn, where the relationship between measured Rn and measured G was established as G = 0.11 Rn - 16.6	Point	30 min
7	NDVI	MODIS NDVI	0.5 km × 0.5 km	16-day composite accessed at daily timescales
8	U_{2m}	ERA5 wind speed at 10 m height scaled to measurement height	31 km × 31 km	Hourly
9	u_{star}	$u_{star} = 0.15\ U_{2m}$	31 km × 31 km	Hourly
10	T_a	ERA5 reanalysis	31 km × 31 km	Hourly
11	RH	ERA5 reanalysis	31 km × 31 km	Hourly

module pwlf (piecewise linear fit). This method fits multiple linear segments to the data while estimating the breakpoint location that minimizes the overall sum of squared residuals. The breakpoint represents a statistically optimal change point where the ET-soil moisture relationship shifts, indicating a transition between soil moisture–limited and energy-limited regimes. This piecewise regression approach provides an objective estimate of soil moisture thresholds without assuming a predefined breakpoint location.

3. Results

3.1. Measured maize field ET

Results from two years of direct rainfall measurements (Fig. 4a) indicate that the frequency, intensity, and timing of the long rains differed between 2019 and 2020, producing distinct ET dynamics (Fig. 4b). In 2019, rainfall was less frequent but more intense, with daily totals reaching up to 72 mm. Correspondingly, ET rose from near-zero at planting (April 12) to a maximum about 25 days later, then steadily declined over the remainder of the 50-day growing period. In contrast, 2020 experienced more frequent but lower magnitude rainfall events (0.2–36.5 mm day^{-1}) with no discernible pattern in their progression. Cumulatively, rainfall during the growing season totalled 221 mm in 2019 and 186 mm in 2020. Also, in 2019, the onset of major rainfall was delayed, misaligning with the widely reported onset time, but aligned with sowing, while in 2020, rains arrived on time but were insignificant, delaying sowing beyond the usual window. Ultimately, direct ET measurements showed that the total ET of the growing season was 221 mm in 2019 and 269 mm in 2020 despite a lower total rainfall in 2020. At the growth stage level, in 2019, ET increased from the early to late vegetative stage and then declined during the reproductive stage, whereas in 2020 it decreased from the early to late vegetative stage and declined further during the reproductive stage (Table 3).

Expanding on the rainfall dynamics, field measurements reveal that pre-sowing SMC and rainfall coupled with post-sowing rainfall patterns

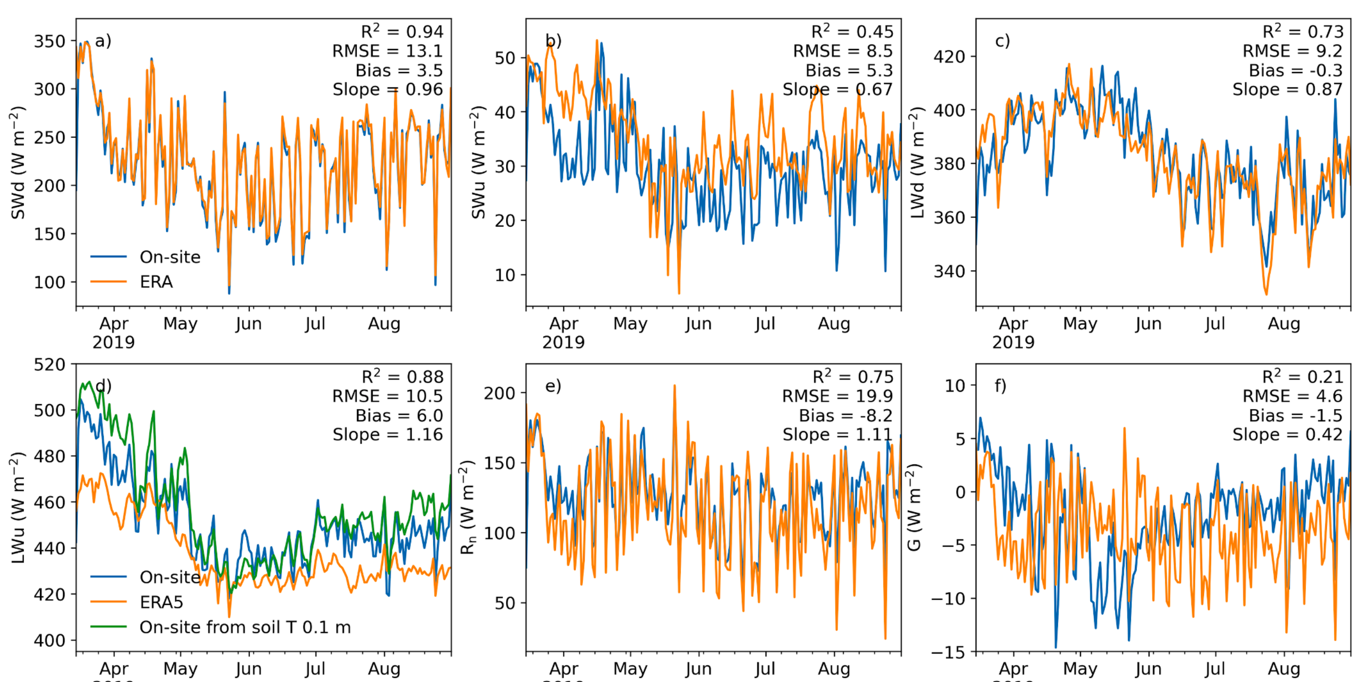

Fig. 3. Comparison of on-site measured radiative components, SEBS model inputs (Table 2) and ERA5 reanalysis components for growing season 2019. (a) downward shortwave radiation (SWd), (b) upward shortwave radiation (SWu), (c) downward longwave radiation (LWd), (d) upward longwave radiation (LWu), (e) net radiation (Rn), and (f) soil heat flux (G). For each panel, root-mean square error (RMSE), R^2, mean bias error, and linear regression slope are reported with on-site measurements treated as the reference. In panel d), the statistics quantify the relationship between on-site measured LWu and LWu derived from on-site soil temperature.

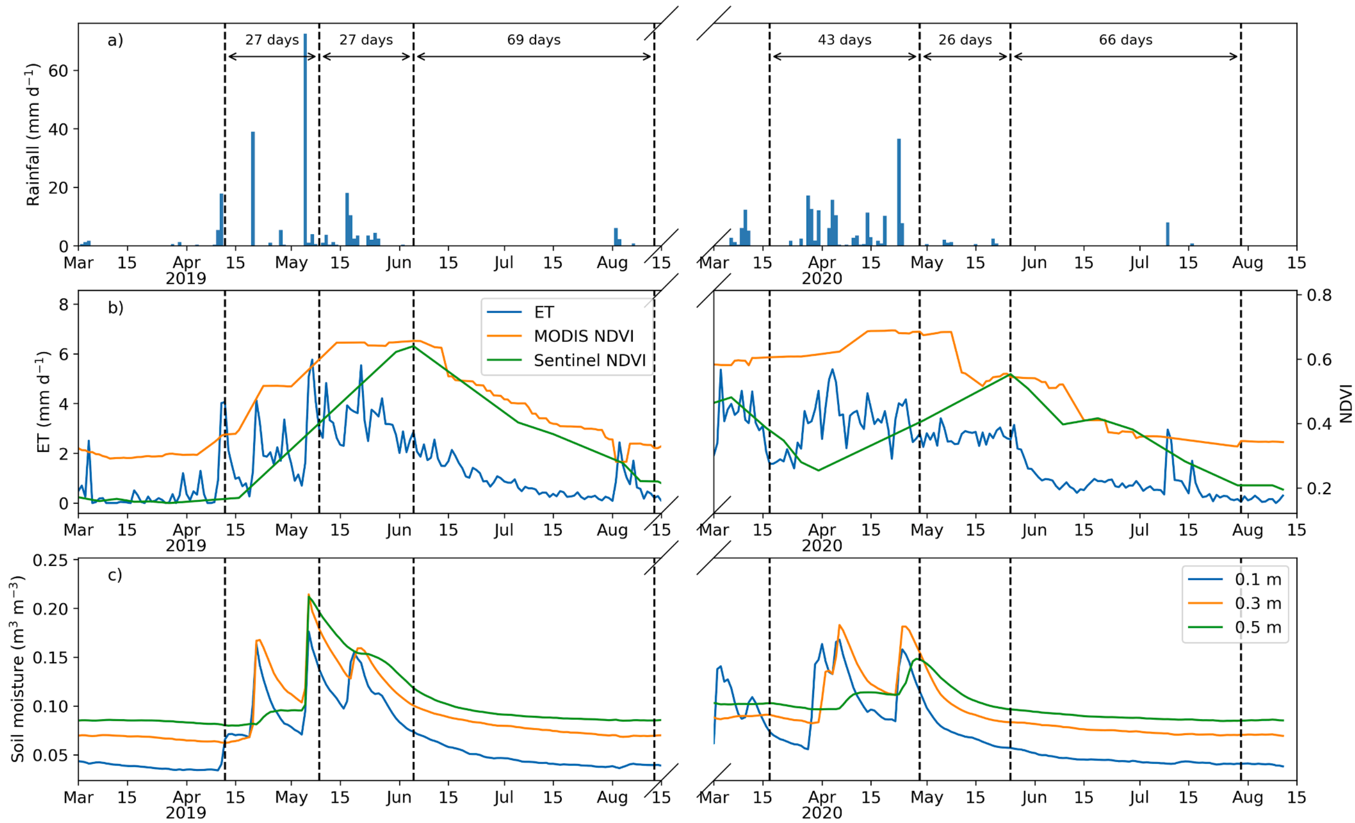

Fig. 4. Daily total rainfall, total evapotranspiration (ET), mean MODIS and Sentinel NDVI, and mean soil moisture content (at 0.1, 0.3, and 0.5 m depths) at growing seasons 2019 and 2020. Maize growth stages (Table 1) are marked by vertical dashed lines, along with the length of each stage.

Table 3
Mean daily ET and standard deviation during each growth stage. Crop growth stages as BBCH scale.

Year	Growth Stage	Mean Daily ET (mm day^{-1})	BBCH scale
2019	early vegetative	2.2 ± 1.4	00–39
2019	late vegetative	3.2 ± 0.8	51–69
2019	reproductive	0.9 ± 0.7	70–99
2020	early vegetative	3.1 ± 1.0	00–39
2020	late vegetative	2.7 ± 0.3	51–69
2020	reproductive	0.85 ± 0.66	70–99

influence soil wetting at different depths, with the top 0.1 m layer ($SMC_{0.1\ m}$) being the most direct link to ET (Fig. 4c). The pre-sowing period in 2019 was characterized by an absence of significant rainfall events, lower NDVI values, and reduced $SMC_{0.1m}$. In contrast, the week before sowing in 2020 experienced a total of 18 mm of rainfall, exhibited elevated NDVI and increased soil moisture content at the same depth (Fig. 4a-c). Peak daily ET variations are strongly correlated with $SMC_{0.1m}$ (Fig. 4b–c), although smaller ET fluctuations associated with radiative variability are not captured by the soil moisture data. Post–sowing observations during the 2019 growing season, show three significant rainfall events coinciding with peak daily ET rates and peak SMC levels at the 0.1 m and 0.3 m depths. In contrast, peak ET rates in 2020 do not align with the major rainfall events but they align with the peak $SMC_{0.1\ m}$ and $SMC_{0.3\ m}$ depths, indicating the influence of initial wetting before sowing (Fig. 4a-c). $SMC_{0.5\ m}$ ranges between 0.09 to 0.11 m^3 m^{-3} for both 2019 and 2020 pre-sowing periods and it remained stable throughout the season, fluctuating only during significant rainfall events (P = 70 mm day^{-1}), with greater variation observed in 2019, (Fig. 4c).

3.2. Soil moisture controls on ET and VPD controls on G_s

3.2.1. ET vs SMC

ET increased linearly with $SMC_{0.1m}$ up to critical thresholds (θ_{crit}) of 0.049 m^3 m^{-3} in the early vegetative stage (R^2=0.86), 0.068 m^3 m^{-3} in the late vegetative stage (R^2=0.94), and 0.056 m^3 m^{-3} in the reproductive stage (R^2=0.44; all $p < 0.001$) (Fig. 5a, Table 4). These θ_{crit} thresholds corresponded to ET values of approximately 1.1 mm d^{-1} in the early vegetative stage, 2.7 mm d^{-1} in the late vegetative stage, and 2.1 mm d^{-1} in the reproductive stage. Comparison across soil moisture depths shows that ET was most tightly correlated with soil moisture at 0.1 m depth ($R^2 = 0.83$), with weaker relationships at 0.3 m ($R^2 = 0.73$) and 0.5 m ($R^2 = 0.71$) over the approximately linear range (Fig. S3).

3.2.2. ET vs SMP

In the early vegetative and reproductive stages, the ET-$\Psi_{0.1\ m}$ relationship was characterized by a biphasic, inflected curve while during the late vegetative stage, this relationship exhibited two distinct clusters—enclosed by the dashed orange circles labelled A and B—which corresponded to aggregations of ET observations at the extremes of the $\Psi_{0.1\ m}$ gradient (Fig. 5b, Table 4). Specifically for the early vegetative and reproductive growth stages, as the $\Psi_{0.1\ m}$ declined below 0 MPa, ET rapidly decreased until the first inflection point was reached after which the rate of decline slowed markedly until the second inflection point, beyond which ET again decreased rapidly with further reductions in $\Psi_{0.1\ m}$. Notably, the ET_{crit} values identified in Fig. 5a corresponded to intersections on the ET–$\Psi_{0.1m}$ curve at critical soil matric potential (Ψ_{crit}) values of approximately –1.5 MPa for the early vegetative stage ($R^2 = 0.89$, $p < 0.001$) and –1.3 MPa for the reproductive stage ($R^2 = 0.75$, $p < 0.001$) (Table 4).

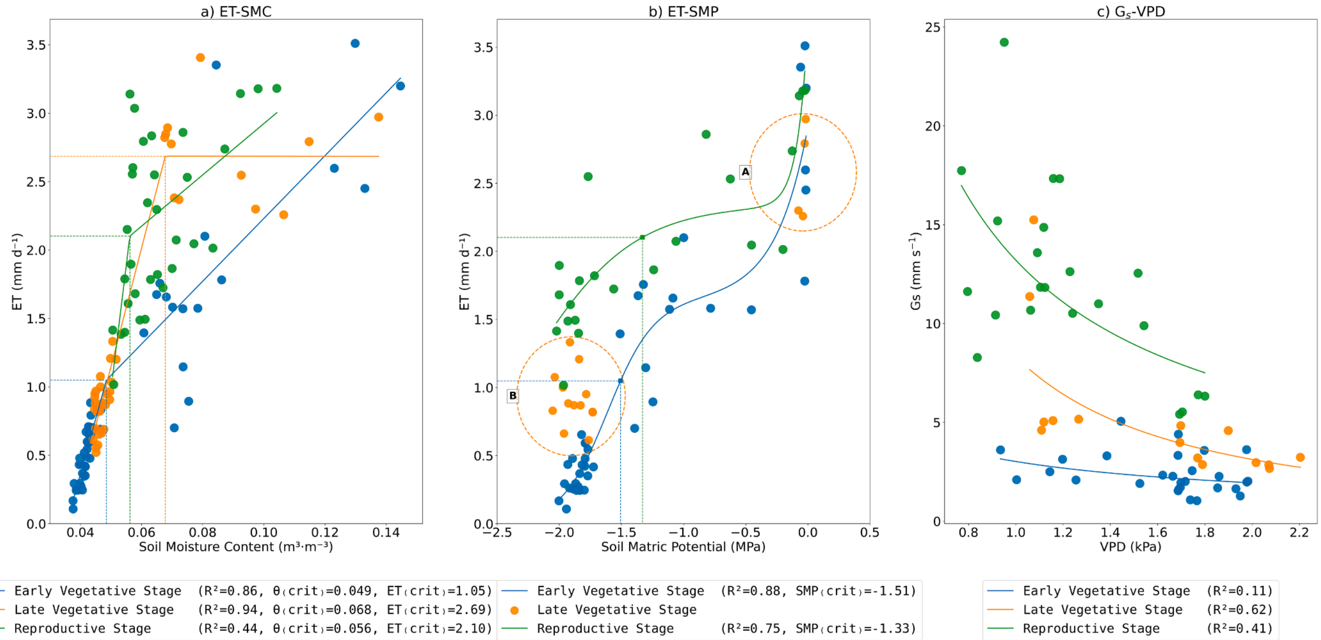

Fig. 5. Relationships between ecosystem fluxes and environmental driver using data from the 2019 and 2020 growing seasons: (a) daily measured evapotranspiration (ET) versus soil moisture content (SMC) at 0.1 m depth, (b) daily ET versus soil matric potential (SMP) at 0.1 m depth, and (c) midday stomatal conductance (G_s, Eq. (1)) versus vapor pressure deficit (VPD). Data from days with rainfall exceeding 0.5 mm were excluded, and NDVI values are derived from Sentinel-2 imagery. No continuous fit is shown for the late vegetative stage in panel (b) due to insufficient and clustered data points. All p-values are < 0.001 except for the early vegetative and reproductive stage in panel (c). See Table 4 for statistics of the fitted equations.

Table 4
Summary of fitted equations and parameters by growth stage. Piecewise linear (Panel a), logistic–exponential (Panel b), and power-law (Panel c) functions were fitted. Parameters a, b, a_1, b_1, c_1, a_2, b_2, and w_1 are regression coefficients estimated from the respective fits. θ_{crit} denotes critical soil moisture content and ET denotes evapotranspiration value at θ_{crit}, while SMP_{crit} denotes the critical soil matric potential. Each fit includes parameter estimates, the coefficient of determination (R^2), and the associated p-value.

Panel	Growth Stage	Fitted Equation	Parameters	R^2	p-value
a	Early Vegetative Stage (ET vs SMC)	Piecewise linear: $ET = \begin{cases} a_1 \cdot SMC + b_1, & \text{if } SMC < \theta_{crit} \\ a_2 \cdot SMC + b_2, & \text{if } SMC \geq \theta_{crit} \end{cases}$	$a_1 = 80.83$, $b_1 = -2.87$; $a_2 = 22.94$, $b_2 = -0.06$; $\theta_{crit} = 0.049$ $m^3\ m^{-3}$; ET = 1.05 mm D^{-1}	0.862	< 0.001
	Late Vegetative Stage (ET vs SMC)	Piecewise linear: $ET = \begin{cases} a_1 \cdot SMC + b_1, & \text{if } SMC < \theta_{crit} \\ a_2 \cdot SMC + b_2, & \text{if } SMC \geq \theta_{crit} \end{cases}$	$a_1 = 86.62$, $b_1 = -3.19$; $a_2 = -0.02$, $b_2 = 2.69$; $\theta_{crit} = 0.068$ $m^3\ m^{-3}$; ET = 2.69 mm D^{-1}	0.936	< 0.001
	Reproductive Stage (ET vs SMC)	Piecewise linear: $ET = \begin{cases} a_1 \cdot SMC + b_1, & \text{if } SMC < \theta_{crit} \\ a_2 \cdot SMC + b_2, & \text{if } SMC \geq \theta_{crit} \end{cases}$	$a_1 = 182.08$, $b_1 = -8.13$; $a_2 = 18.75$, $b_2 = 1.05$; $\theta_{crit} = 0.056$ $m^3\ m^{-3}$; ET = 2.10 mm D^{-1}	0.437	< 0.001
b	Early Vegetative Stage (ET vs SMP)	Mixed logistic + exponential decay: $ET = w_1 \cdot \left[\frac{c_1}{1 + exp(-a_1 \cdot (SMP - b_1))}\right] + (1 - w_1) \cdot [a_2 \cdot exp(b_2 \cdot SMP)]$	a_1=5.38, b_1=−1.61, c_1=3.21, a_2=2.59, b_2=3.83, w_1=0.51; ET =1.05 mm·d^{-1}, SMP_{crit} =−1.51 MPa	0.885	< 0.001
	Late Vegetative Stage (ET vs SMP)	Clustering analysis (no continuous fit)	N/A	N/A	N/A
	Reproductive Stage (ET vs SMP)	Mixed logistic + exponential decay: $ET = w_1 \cdot \left[\frac{c_1}{1 + exp(-a_1 \cdot (SMP - b_1))}\right] + (1 - w_1) \cdot [a_2 \cdot exp(b_2 \cdot SMP)]$	a_1=2.37, b_1=−2.25, c_1=3.49, a_2=4.01, b_2=11.89, w_1=0.67; ET =2.10 mm·d^{-1}, SMP_{crit}=−1.33 MPa	0.751	< 0.001
c	Early Vegetative Stage (G_s vs VPD)	Power-law: $G_s = a \cdot (VPD)^b$	a = 6.00, b = −1.10	0.150	> 0.001
	Late Vegetative Stage (G_s vs VPD)	Power-law: $G_s = a \cdot (VPD)^b$	a = 8.32, b = −1.41	0.617	< 0.001
	Reproductive Stage (G_s vs VPD)	Power-law: $G_s = a \cdot (VPD)^b$	a = 13.20, b = −0.96	0.408	> 0.001

3.2.3. G_s vs VPD

Fig. 5c shows mean surface conductance (G_s) versus midday vapor pressure deficit (VPD; averaged from 10:00 to 14:00) across growth stages. G_s is consistently low (0–5 mm s^{-1}) in the early vegetative stage, showing only a weak response to rising VPD (R^2=0.15). In the late vegetative stage, G_s declines sharply with VPD, giving the strongest relationship (R^2=0.62). The reproductive stage shows an intermediate response (R^2=0.41; all p < 0.001) that is stronger than in the early vegetative stage (Fig. 5c, Table 4).

3.3. SEBS model ET

The SEBS modelled ET (ET_{SEBS}), estimated using on-site measured radiative inputs, closely aligns with the measured ET during the 2019 growing season (R^2 = 0.91, RMSE = 0.68 mm day^{-1}, Fig. 6a-b). The SEBS model demonstrates mixed performance, effectively capturing the overall measured ET trend while slightly overestimating peak ET values following rainfall events. Notably, significant overestimations occur at the lowest measured ET values during the early and late stages of the 2019 growing season.

ET_{SEBS} parametrized with a combination of on-site measured input and ERA5 reanalysis data (Table 2) for the long-term analysis was linearly related to the measured ET for the 2019 and 2020 growing seasons (R^2 = 0.64, RMSE = 1.3 mm day^{-1}, Fig. 6c-d). ET_{SEBS} captures well the early season measured ET while overestimating the late season measured ET in 2019. In 2020, the ET_{SEBS} is a large overestimate during the early and mid-season. In general, the ET_{SEBS} has larger day-to-day variability than the SEBS model ET using the on-site measured radiative input. However, ET_{SEBS} captures well the seasonal trends in ET for both seasons.

3.4. Seasonal interannual variability of maize field ET

Seasonal and interannual variability of ET_{SEBS} was analyzed together with the measured rainfall and $SMC_{0.1m}$ for growing seasons 2014 to 2022. The growing season ET_{SEBS} ranged from 94 to 408 mm season^{-1} (Table 5). Growing season rainfall was positively related to growing season ET_{SEBS} (Fig. 7a). However, in two seasons (2018 and 2020), ET_{SEBS} was anomalously high relative to rainfall. This resulted in large negative $P - -ET_{SEBS}$ and weakened the overall relationship between rainfall and ET_{SEBS}. The mean growing season $P - ET_{SEBS}$ was -80 ± 82 mm season^{-1}. The mean growing season rainfall was 190 $\pm$ 63 mm season^{-1} and ET_{SEBS} was 270 $\pm$ 99 mm season^{-1} for nine years. The mean soil moisture and max MODIS NDVI had similar linear correlation with the growing season ET_{SEBS} ($R^2 = 0.46$, p-value = 0.04; $R^2 = 0.51$, p-value = 0.03) (Fig. 7b-c). $SMC_{0.1m}$ at the beginning of the growing season ranged from 0.03 to 0.18, while $SMC_{0.1m}$ at the end of the season was constant at 0.04 (Table 5).

The peaks in daily ET_{SEBS} consistently followed the increases in $SMC_{0.1m}$ across all the years, underscoring the strong influence of rainfall variability on seasonal soil moisture and ET dynamics (Fig. S7). The seasonal changes follow roughly three patterns. In drought year with no major increase in $SMC_{0.1m}$, such as 2022, $SMC_{0.1m}$ remained consistently low, which strongly constrained ET, leading to suppressed fluxes and minimal variability. ET and $SMC_{0.1m}$ stayed low in 2019 before the delayed rainfall but increased sharply once significant rainfall occurred later in the season. All other years were characterized by early-season rainfall that replenished soil moisture and supported strong ET peaks in April – May period, followed by a steady decline of both variables through the growing season as soil water was progressively depleted. During the severe drought year 2022, rainfall was only 68 mm season^{-1} and maximum $SMC_{0.1m}$ was 0.07. Mean daily ET_{SEBS} was 0.56 mm day^{-1} in 2022 compared with 1.39 mm day^{-1} across the other years, reflecting substantially reduced ET_{SEBS} under drought conditions.

The critical soil moisture threshold was determined for each growing season using ET_{SEBS} and $SMC_{0.1m}$ and $SMC_{0.3m}$ (Fig. S3, S4 and Table 5). The fitted growing-season $\theta_{crit,0.1\ m}$ derived with ET_{SEBS} varied from 0.04 to 0.09 and $\theta_{crit,0.3\ m}$ varied from 0.09 to 0.12 across years exhibiting the expected ET–soil moisture response (Table 5). The $\theta_{crit,0.3\ m}$ values were on average 0.04 higher than the $\theta_{crit,0.1\ m}$ (Table 5). Comparison of the wet years show that there is variability between the different wet years in the initial slope and in the upper ET levels reached at high soil moisture between the years (Fig. 8). During individual wet years, $ET_{SEBS}-SMC_{0.1m}$ relationship showed the expected pattern with linearly increasing ET up to the water-stress threshold except in 2017 (Fig. S3). In contrast, during the dry years (2021 and 2022), the relationship was linear or nearly flat with lower slope than in wet years (Fig. 8 and S3). There was no relationship between interannual variability in root-zone

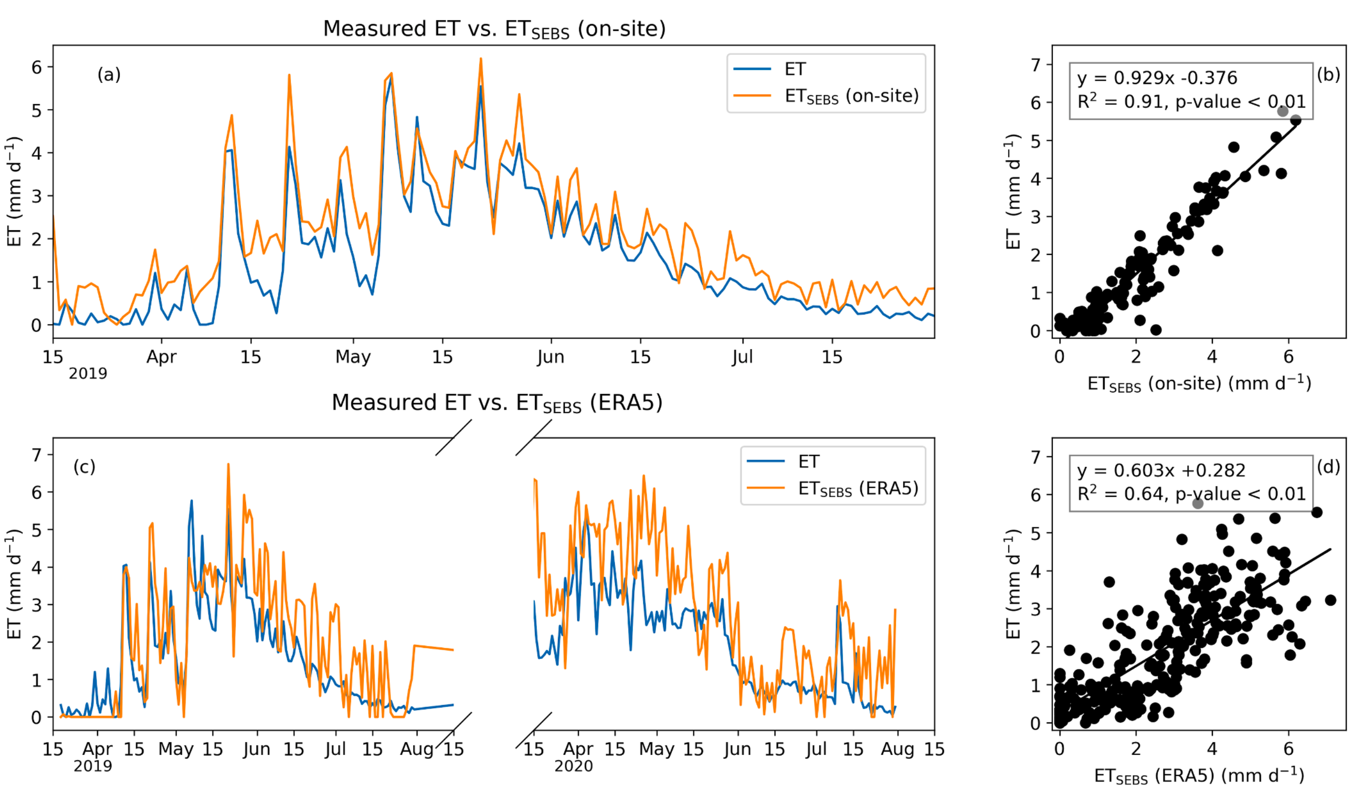

Fig. 6. Time series of daily measured ET and SEBS estimated ET using on-site measured radiative components in 2019 (a) and their relationship (b). Time series of measured ET and SEBS estimated ET using the on-site and ERA5 inputs (Table 2) in 2019 and 2020 (c) and their relationship (d).

Table 5
Growing season rainfall (P), ET_{SEBS}, MODIS $NDVI_{max}$, initial surface soil moisture content (SWC_{init}), and soil moisture content at the end of the season (SWC_{end}) for the years 2014 to 2022. Critical soil moisture thresholds ($\theta_{crit,0.1\ m}$ and $\theta_{crit,0.3\ m}$) were determined each year from ET_{SEBS}-soil moisture relationship (Fig. S4 and S5). The growing season is defined from March 15 to August 15 each year.

Year	P (mm)	ET_{SEBS} (mm)	$NDVI_{max}$	SWC_{init} (m^3/m^3)	SWC_{end} (m^3/m^3)	$\theta_{crit,0.1m}$ (m^3/m^3)	$\theta_{crit,0.3m}$ (m^3/m^3)
2014	302	303	0.61	0.11	0.04	0.07	0.12[a]
2015	199	315	0.50	0.03	0.04	0.08	0.07[a]
2016	226	274	0.51	0.07	0.04	0.09	0.11
2017	168	203	0.63	0.06	0.04	0.09[a]	0.08[a]
2018	175	374	0.73	0.18	0.04	0.08	0.12
2019	221	289	0.66	0.04	0.04	0.04	0.10
2020	186	408	0.69	0.09	0.04	0.06	0.09
2021	161	168	0.58	0.05	0.03	0.04[a]	0.09
2022	68	94	0.35	0.04	0.04	0.07[a]	0.07[a]

[a] In these years, the ET_{SEBS}-soil moisture relationship did not exhibit a clear piecewise linear structure characterized by an initial linear increase.

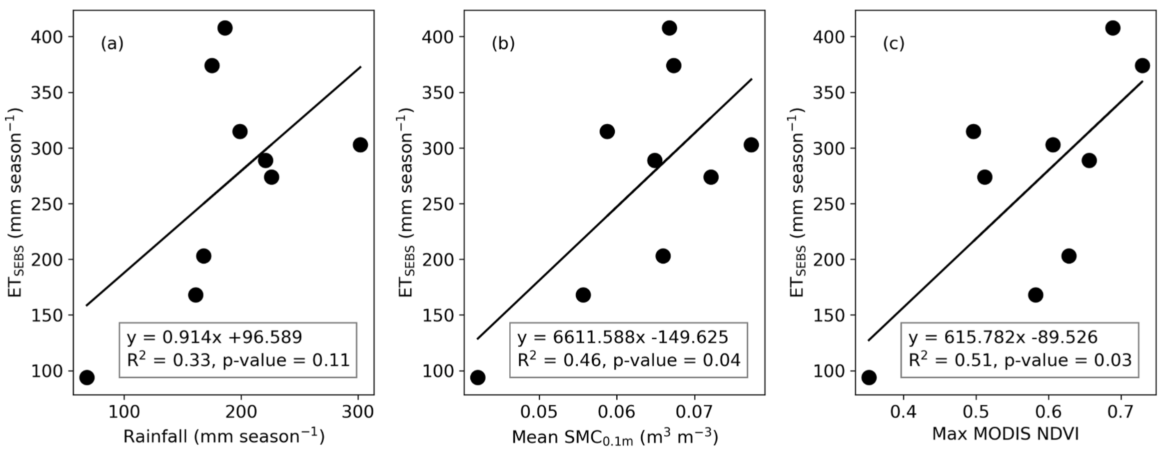

Fig. 7. Relationship between growing season ET_{SEBS}, rainfall (a), mean soil moisture at 0.1 m depth (b) and maximum MODIS NDVI (c). Data from each growing season (March 15–August 15) from 2014 to 2022.

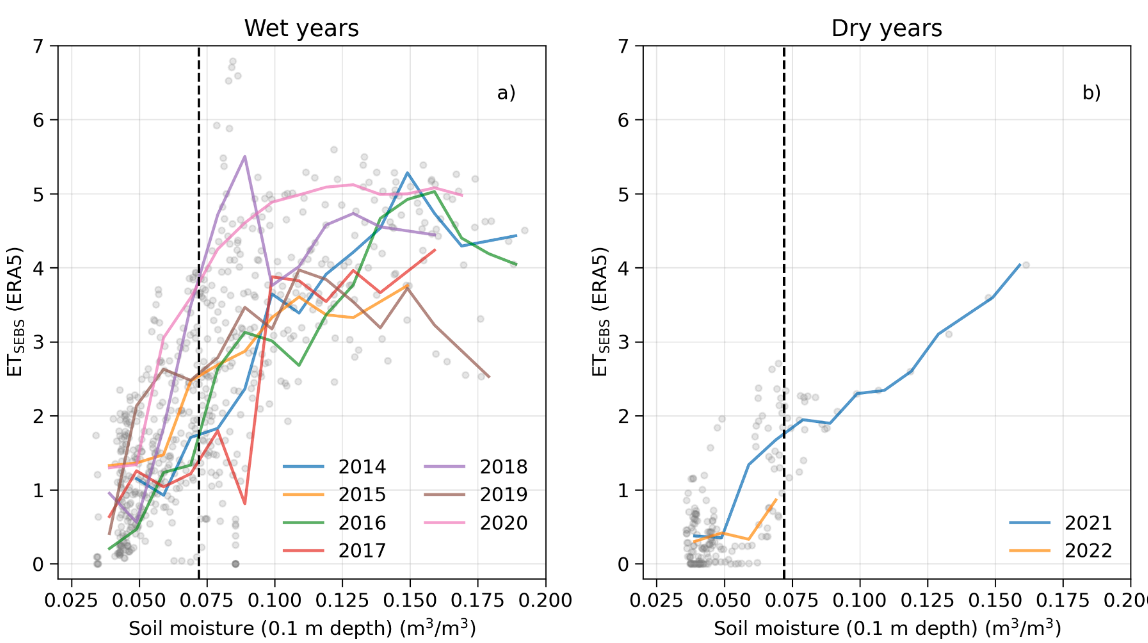

Fig. 8. Relationship between 7-day moving average of ET_{SEBS} and observed soil moisture content at 0.1 m depth in wet (a) and dry (b) years. Gray points indicate daily values. Solid lines show soil-moisture–binned mean ET for visualization of each year. The dashed vertical line indicates the mean critical soil moisture threshold, $\theta_{crit,0.1\ m}$, derived from individual-year fits for wet years (Table 5).

θ_{crit} at 0.1 and 0.3 m depths and total rainfall or NDVI (Fig. S6). However, $\theta_{crit,0.1\ m}$ and $\theta_{crit,0.3\ m}$ were positively related to the early season rainfall (Fig. S6).

4. Discussion

The analysis demonstrates that the critical soil moisture threshold (θ_{crit}) is not a fixed soil hydraulic property but a dynamic threshold that varies with maize growth stage, soil depth, and interannual rainfall conditions. Growth-stage-specific $\theta_{crit,0.1\ m}$ values ranged from 0.05 to 0.07 (Fig. 5), while (add model ET) growing-season $\theta_{crit,0.1\ m}$ derived with ET_{SEBS} varied from 0.04 to 0.09 across years exhibiting the expected ET–soil moisture response (Table 5). This variability indicates that ET sensitivity to soil moisture is strongly state-dependent and reflects changes in crop development and soil–plant hydraulic functioning rather than static soil properties.

The depth dependence of θ_{crit} and ET–soil moisture coupling reveals a vertical separation between stress onset and ET sensitivity. Seasonal pattern of measured ET closely followed soil moisture in the top layers ($SMC_{0.1\ m}$ and $SMC_{0.3\ m}$) in both 2019 and 2020 (Fig. 4b-c), consistent with field observations showing most roots concentrated in this layer (based on field observations; data not shown). The $SMC_{0.1\ m}$ most closely tracked measured ET over the water stress range (Fig. S3). On average, $\theta_{crit,0.3\ m}$ values were 0.04 higher than the $\theta_{crit,0.1\ m}$ values (Table 5). These results indicate that shallow soil moisture primarily tracks daily ET variability, whereas higher critical thresholds at 0.3 m depth likely reflect greater soil water storage at depth rather than a stronger coupling between deeper soil moisture and ET. This distinction is important for the interpretation of ET–soil moisture relationships derived from simplified or spatially aggregated representations of soil water availability.

The deeper soil layer ($SMC_{0.5\ m}$) showed a weak correlation with measured ET, reinforcing the inference that effective maize water uptake was largely confined to the upper soil profile (0.1–0.3 m). This is consistent with previous findings on maize root distribution in semi-arid maize field in Zimbabwe (Chikowo et al., 2003; Nyakudya and Stroosnijder, 2014;). Long-term measurements demonstrate that the initial soil moisture levels range from 0.04 to 0.18 $m^3\ m^{-3}$ (Table 5). This indicates that soils are not necessarily dry at the onset of the growing season. This finding has implications for yield estimation and irrigation planning in this system.

The present study suggests that the ET–$\Psi_{0.1m}$ relationship during the early vegetative and reproductive stages is highly nonlinear, forming a biphasic, inflected curve (Fig. 5b). As soil matric potential drops from 0 MPa, ET decreases sharply, consistent with what is commonly described as Stage I soil evaporation, when water is readily available in large pores (Shahraeeni et al., 2012; Or et al., 2013). When $\Psi_{0.1m}$ falls below roughly –1.0 MPa, the observed decline in ET may reflect a shift toward water being increasingly confined in smaller pores, where vapor diffusion (Stage II evaporation) is thought to dominate (Fig. 5b) (Or et al., 2013). Similarly to the variability of θ_{crit} across growth stages, the critical soil water potential thresholds varied from –1.5 MPa (early vegetative stage) to –1.3 MPa (reproductive stage) (Fig. 5b).

Consistent with these stage-dependent soil moisture and hydraulic controls on ET, surface conductance (G_s) responses to atmospheric demand also varied systematically across maize developmental stages. The surface conductance varied from 5 to 25 mm s^{-1} (Fig. 5c), similar to those observed in irrigated maize in northwestern China (Li et al., 2013) and semi-arid rainfed maize in China's monsoon transition zone (Yue et al., 2022). During early growth stage, surface conductance showed weak sensitivity to vapor pressure deficit, consistent with soil evaporation dominating ET when θ_{crit} values were low (0.05). In contrast, during the late vegetative stage, higher θ_{crit} values (0.07) coincided with increased canopy development and stronger transpiration control of ET, resulted to G_s declining sharply with VPD.

ET magnitude and sensitivity to soil moisture were not uniform across seasons, as evidenced by differences in both the initial ET–soil moisture slope and the upper ET levels reached under high soil moisture conditions (Fig. 8). The cumulative ET for the 2019 and 2020 growing seasons was 221 mm and 269 mm, respectively. These values fall within the range reported for rainfed maize in nearby semi-arid region in Kenya, where Zhang et al. (2020) evaluated different maize mulching strategies using a similar hybrid variety in Kenya and reported maize ET of 225 mm in 2016 and 213 mm in 2017. In addition to the magnitude of ET, the variability in ET sensitivity to soil moisture is consistent with previous studies on maize, as similar growth-stage-dependent changes in ET–soil moisture sensitivity have been reported under controlled irrigation conditions (Xu et al., 2023).

There was no relationship between interannual variability in root-zone θ_{crit} at 0.1 and 0.3 m depths and total rainfall or NDVI (Fig. S6). However, there was a consistent positive relationship with early season rainfall indicating the importance of rainfall timing rather than seasonal totals (Fig. S6). This interpretation is consistent with yield analyses from this site, which showed that maize yield during the long rainy seasons was governed by rainfall temporal distribution rather than total precipitation (Tuure et al., 2025). Years characterized by low yield (2021) and complete crop failure (2022) exhibited a fundamentally different ET–soil moisture regime, with ET remaining linearly water-limited throughout the growing season (Fig. 8). Despite remaining water-limited throughout the season, the dry year 2021 still produced a measurable yield (0.22 t ha^{-1}, Tuure et al., 2025), indicating that residual soil moisture and early-season water availability can sustain limited productivity even under prolonged moisture stress.

Higher early-season rainfall was associated with higher θ_{crit}, indicating that soil water availability during early crop development plays a role in regulating seasonal ET dynamics. This finding underscores the importance of early-season soil water management for drought adaptation and suggests that interventions targeting mid- or late-season water stress alone may be less effective. Six of the nine study years had relatively high early-season soil moisture (see Fig. S7), indicating potential to improve rainwater use efficiency by enhancing the infiltration and retention of early rainfall within the root zone. In this context, on-farm rainwater harvesting measures that reduce early-season soil evaporation, potentially complemented by supplemental drip irrigation where feasible, could help convert a greater fraction of early rainfall into productive soil water storage during critical phases of maize development.

Furthermore, the occurrence of high early-season rainfall followed by prolonged dry periods may have contrasting effects on crop resilience. Abundant surface moisture can promote shallow root development, which later limits access to deeper soil water. While rooting depth was not explicitly assessed in this study, the observed sensitivity of θ_{crit} to early-season rainfall underscores the need for future investigations that explicitly couple root system development with soil moisture dynamics and ET responses under variable rainfall.

Growing season rainfall was positively related to ET_{SEBS}, indicating that interannual variability in ET_{SEBS} was generally constrained by water availability (Fig. 7). The 9-year mean P – ET_{SEBS} was -80 ± 82 mm $season^{-1}$. Direct comparison with measured ET in 2020 showed that ET_{SEBS} was consistently overestimated during the early and mid-growing season (Fig. 6c). A similar pattern was observed in 2018, when ET_{SEBS} remained persistently above 4 mm day^{-1} throughout much of the growing season (Fig. S7). Similar overestimation in ET_{SEBS} under dry and sparsely vegetated conditions has been reported in other studies (Gokmen et al., 2012; Huang et al., 2015). In addition, uncertainties in the ERA5 radiative inputs used as input for the SEBS model may have contributed to elevated ET estimates. The RMSE of daily ET for the SEBS model ET using the on-site measured radiative input was 0.68 mm day^{-1} and 1.3 mm day^{-1} for ET_{SEBS}. These are lower than the RMSE values of 2.2 mm day^{-1} for SEBS ET compared to ET measured using the surface renewal technique at an irrigated sugar cane field in South Africa (Gokool et al., 2016). Our RMSE values were higher than the SEBS ET with an RMSE value of 0.21 mm day^{-1} for forest ET at Qilian mountains in China (Tian et al., 2015). Overall, these results suggest that the quality of SEBS ET depends on the quality of the input data and that there is a tendency to overestimate ET under bare soil conditions.

5. Conclusion

This study shows that the ET responses of rainfed semi-arid maize crops, ranging from wet years to years of crop failure, cannot be adequately described using fixed soil moisture thresholds. ET dynamics differed substantially between years, reflecting pronounced interannual variability in both the magnitude of ET and its sensitivity to soil moisture availability. ET sensitivity reflects shifts in crop developmental stage and root-zone water availability shaped by rainfall timing, with important implications for managing drought risk. The identification of growth-stage- and depth-dependent critical soil moisture and matric potential thresholds highlights that maize water use sensitivity evolves throughout the season in response to changing canopy and hydraulic conditions. These findings underscore the importance of accounting for state-dependent soil moisture thresholds when interpreting ET responses and suggest that strategies enhancing early-season soil water retention may improve resilience of rainfed maize systems under increasing rainfall variability.

CRediT authorship contribution statement

Matti Räsänen: Writing – review & editing, Writing – original draft, Visualization, Software, Project administration, Methodology, Data curation, Conceptualization. **Julius Omondi:** Writing – review & editing, Writing – original draft, Methodology, Conceptualization. **Vincent Odongo:** Writing – review & editing, Methodology, Conceptualization. **Temesgen Abera:** Writing – review & editing, Methodology. **Juuso Tuure:** Writing – review & editing. **Janne Heiskanen:** Writing – review & editing, Methodology. **Cheng-I Hsieh:** Writing – review & editing, Methodology. **Laura Alakukku:** Writing – review & editing, Funding acquisition. **Lutz Merbold:** Writing – review & editing. **Petri Pellikka:** Writing – review & editing, Funding acquisition. **Timo Vesala:** Writing – review & editing, Supervision, Funding acquisition.

Declaration of competing interest

The authors declare that they have no known competing financial interests or personal relationships that could have appeared to influence the work reported in this paper.

Acknowledgements

This work was supported by the University of Helsinki and the Research Council of Finland projects SMARTLAND (Environmental sensing of ecosystem services for developing climate-smart landscape framework to improve food security in East Africa, decision no. 318645) and REACT (Regenerative agricultural systems for climate resilience in agroecological gradient in East Africa, decision no. 351087), Research Council of Finland University Profiling funding InterEarth (grant no. 353218), the European Union DG International Partnerships under the DeSIRA program (FOOD/2020/418-132) through the ESSA (Earth observation and environmental sensing for climate-smart sustainable agropastoral ecosystem transformation in East Africa) project and ICOS-FIRI and ICOS-Finland via University of Helsinki funding. The research was conducted under research permits from the National Commission for Science, Technology and Innovation of Kenya NACOSTI P/18/97336/26355 and NACOSTI/P/24/34925. We wish to thank the staff of the Taita Research Station of the University of Helsinki in Kenya. The authors thank the farmers Francis Mwasofi and Mwadime Mjomba for their help with the field work and maintenance of the instruments.

Supplementary materials

Supplementary material associated with this article can be found, in the online version, at doi:10.1016/j.agrformet.2026.111219.

Data availability

Data will be made available on request.

References

Acharya, B., Sharma, V., 2021. Comparison of satellite driven surface energy balance models in estimating crop evapotranspiration in semi-arid to arid inter-mountain region. Remote Sens. (Basel) 13, 1822.
Allen, R.G., Pereira, L.S., Raes, D., Smith, M., others, 1998. Crop Evapotranspiration-Guidelines For Computing Crop Water requirements-FAO Irrigation and Drainage Paper 56, 300. Fao, Rome, D05109.
Aubinet, M., Vesala, T., Papale, D. (Eds.), 2012. Eddy covariance: a Practical Guide to Measurement and Data Analysis. Springer Science & Business Media.
Bastiaanssen, W.G., Menenti, M., Feddes, R.A., Holtslag, A.A.M., 1998. A remote sensing surface energy balance algorithm for land (SEBAL). 1. formulation. J Hydrol 212-213, 198–212. https://doi.org/10.1016/S0022-1694(98)00253-4.
Chen, J.M., Liu, J., 2020. Evolution of evapotranspiration models using thermal and shortwave remote sensing data. Remote Sens. Environ. 237, 111594. https://doi.org/10.1016/j.rse.2019.111594.
Chen, X., Su, Z., Ma, Y., Yang, K., Wen, J., Zhang, Y., 2013. An improvement of roughness height parameterization of the Surface Energy Balance System (SEBS) over the Tibetan plateau. J. Appl. Meteorol. Climatol. 52 (3), 607–622.
Chikowo, R., Mapfumo, P., Nyamugafata, P., Nyamadzawo, G., Giller, K.E., 2003. Nitrate-N dynamics following improved fallows and maize root development in a Zimbabwean sandy clay loam. Agrofor. Syst. 59 (3), 187–195.
Dowling, T.P.F., Langsdale, M.F., Ermida, S.L., Wooster, M.J., Merbold, L., Leitner, S., Trigo, I.F., Gluecks, I., Main, B., O'Shea, F., Hook, S., Rivera, G., De Jong, M.C., Nguyen, H., Hyll, K., 2022. A new East African satellite data validation station: performance of the LSA-SAF all-weather land surface temperature product over a savannah biome. ISPRS J. Photogramm. Remote Sens. 187, 240–258.
Elkatoury, A., Alazba, A.A., Radwan, F., Kayad, A., Mossad, A., 2024. Evapotranspiration estimation assessment using various satellite-based surface energy balance models in arid climates. Earth. Syst. Environ. 1–23.
García-Gutiérrez, V., Stöckle, C., Gil, P.M., Meza, F.J., 2021. Evaluation of penman-monteith model based on sentinel-2 data for the estimation of actual evapotranspiration in vineyards. Remote Sens. (Basel) 13, 478. https://doi.org/10.3390/rs13030478.
Gokmen, M., Vekerdy, Z., Verhoef, A., Verhoef, W., Batelaan, O., van der Tol, C., 2012. Integration of soil moisture in SEBS for improving evapotranspiration estimation under water stress conditions. Remote Sens. Environ. 121, 261–274.
Gokool, S., Chetty, K., Jewitt, G., Heeralal, A., 2016. Estimating total evaporation at the field scale using the SEBS model and data infilling procedures. Water Sa 42, 673.
Hersbach, H., Bell, B., Berrisford, P., Hirahara, S., Horányi, A., Muñoz-Sabater, J., Nicolas, J., Peubey, C., Radu, R., Schepers, D., Simmons, A., Soci, C., Abdalla, S., Abellan, X., Balsamo, G., Bechtold, P., Biavati, G., Bidlot, J., Bonavita, M., De Chiara, G., Dahlgren, P., Dee, D., Diamantakis, M., Dragani, R., Flemming, J., Forbes, R., Fuentes, M., Geer, A., Haimberger, L., Healy, S., Hogan, R.J., Hólm, E., Janisková, M., Keeley, S., Laloyaux, P., Lopez, P., Lupu, C., Radnoti, G., de Rosnay, P., Rozum, I., Vamborg, F., Villaume, S., Thépaut, J.-N., 2020. The ERA5 global reanalysis. Quarterly J. Royal Meteorol. Soc. 146, 1999–2049. https://doi.org/10.1002/qj.3803.
Huang, C., Li, Y., Gu, J., Lu, L., Li, X., 2015. Improving estimation of evapotranspiration under water-limited conditions based on SEBS and MODIS data in arid regions. Remote Sens. (Basel) 7 (12), 16795–16814.
Huang, H., Huang, Y., 2023. Radiative sensitivity quantified by a new set of radiation flux kernels based on the ECMWF reanalysis v5 (ERA5). Earth. Syst. Sci. Data 15, 3001–3021.
Kljun, N., Calanca, P., Rotach, M.W., Schmid, H.P., 2015. A simple two-dimensional parameterisation for flux footprint prediction (FFP). Geosci. Model. Dev. 8, 3695–3713. https://doi.org/10.5194/gmd-8-3695-2015.
Krell, N.T., Morgan, B.E., Gower, D., Caylor, K.K., 2021. Consequences of dryland maize planting decisions under increased seasonal rainfall variability. Water. Resour. Res. 57, e2020WR029362. https://doi.org/10.1029/2020WR029362.
Leclerc, C., Mwongera, C., Camberlin, P., Moron, V., 2014. Cropping system dynamics, climate variability, and seed losses among east african smallholder farmers: a retrospective survey. Weather, Climate, Soc. 6, 354–370. https://doi.org/10.1175/WCAS-D-13-00035.1.
Li, S., Kang, S., Zhang, L., Li, F., Du, T., Tong, L., Wang, S., Lu, H., 2013. Greater effect of canopy conductance in regulating the energy partition above the maize field in arid northwest china. Hydrol. Process. 27, 3452–3460.
Marimi, A.M., 1979. Dryland Farming in kenya: Problems and Prospects. Institute for Development Studies, University of Nairobi.
Mauder, M. and Foken, T.: Documentation and instruction manual of the eddy covariance software package TK2, Technical Report, Universität Bayreuth, Abteilung Mikrometeorologie, Bayreuth, Germany, 2004.
Meier, U. (2018). *Growth stages of mono-and dicotyledonous plants*.
Massman, W.J., 2000. A simple method for estimating frequency response corrections for eddy covariance systems. Agric. For. Meteorol. 104 (3), 185–198.
Moncrieff, J., Clement, R., Finnigan, J., Meyers, T., 2004. Averaging, detrending, and filtering of eddy covariance time series. In: Handbook of micrometeorology: A guide

for surface flux measurement and analysis. Springer Netherlands, Dordrecht, pp. 7–31.

Mwalusepo, S., Massawe, E.S., Affognon, H., Okuku, G.O., Kingori, S., Mburu, P.D., Le Ru, B.P., 2015. Smallholder farmers' perspectives on climatic variability and adaptation strategies in east africa: the case of mount kilimanjaro in tanzania, taita and machakos hills in kenya. https://doi.org/10.4172/2157-7617.1000313.

Nicholson, S.E., 2017. Climate and climatic variability of rainfall over eastern africa. Rev. Geophys. 55, 590–635. https://doi.org/10.1002/2016RG000544.

Norman, J.M., Kustas, W.P., Humes, K.S., 1995. Source approach for estimating soil and vegetation energy fluxes in observations of directional radiometric surface temperature. Agric. For. Meteorol. 77, 263–293. https://doi.org/10.1016/0168-1923(95)02265-Y.

Nyakudya, I.W., Stroosnijder, L., 2014. Effect of rooting depth, plant density and planting date on maize (Zea mays L.) yield and water use efficiency in semi-arid Zimbabwe: modelling with AquaCrop. Agric. Water. Manage. 146, 280–296.

Omondi, J., 2025. Illustration of adopted maize growth stages. created in BioRender. https://BioRender.com/y6rhon2.

Or, D., Lehmann, P., Shahraeeni, E., Shokri, N., 2013. Advances in soil evaporation physics—a review. Vadose Zone J. 12, 1–16.

Pervez, S., McNally, A., Arsenault, K., Budde, M., Rowland, J., 2021. Vegetation monitoring optimization with normalized difference vegetation index and evapotranspiration using remote sensing measurements and land surface models over east africa. Front. Clim. 3, 589981. https://doi.org/10.3389/fclim.2021.589981.

Räsänen, M., Merbold, L., Vakkari, V., Aurela, M., Laakso, L., Beukes, J.P., Zyl, P.G.V., Josipovic, M., Feig, G., Pellikka, P., Rinne, J., Katul, G.G., 2020. Root-zone soil moisture variability across African savannas: from pulsed rainfall to land-cover switches. Ecohydrology 13, e2213. https://doi.org/10.1002/eco.2213.

Raun, W.R., Solie, J.B., Martin, K.L., Freeman, K.W., Stone, M.L., Johnson, G.V., Mullen, R.W., 2005. Growth stage, development, and spatial variability in corn evaluated using optical sensor readings. J. Plant Nutr. 28 (1), 173–182.

Reichstein, M., Falge, E., Baldocchi, D., Papale, D., Aubinet, M., Berbigier, P., Bernhofer, C., Buchmann, N., Gilmanov, T., Granier, A., Grünwald, T., Havránková, K., Ilvesniemi, H., Janous, D., Knohl, A., Laurila, T., Lohila, A., Loustau, D., Matteucci, G., Meyers, T., Miglietta, F., Ourcival, J.-M., Pumpanen, J., Rambal, S., Rotenberg, E., Sanz, M., Tenhunen, J., Seufert, G., Vaccari, F., Vesala, T., Yakir, D., Valentini, R., 2005. On the separation of net ecosystem exchange into assimilation and ecosystem respiration: review and improved algorithm. Glob. Chang. Biol. 11, 1424–1439. https://doi.org/10.1111/j.1365-2486.2005.001002.x.

Salami, A., Kamara, A.B., Brixiova, Z., 2010. Smallholder Agriculture in East africa: Trends, Constraints and Opportunities. African Development Bank, Tunis, Tunisia.

Shahraeeni, E., Lehmann, P., Or, D., 2012. Coupling of evaporative fluxes from drying porous surfaces with air boundary layer: Characteristics of evaporation from discrete pores. Water Resources Research 48 (9).

Shilomboleni, H., Epstein, G., Mansingh, A., 2024. Building resilience in africa's smallholder farming systems: contributions from agricultural development interventions—a scoping review. Ecol. Soc. 29. https://doi.org/10.5751/ES-15373-290322.

Sinergise Solutions d.o.o., 2024. *EO Browser* [web application]. planet labs. Retrieved November 2024, from. https://apps.sentinel-hub.com/eo-browser/.

Su, Z., 2002. The Surface Energy Balance System (SEBS) for estimation of turbulent heat fluxes. Hydrol. Earth. Syst. Sci. 6, 85–100. https://doi.org/10.5194/hess-6-85-2002.

Tian, X., Van der Tol, C., Su, Z., Li, Z., Chen, E., Li, X., Yan, M., Chen, X., Wang, X., Pan, X., 2015. and others: simulation of forest evapotranspiration using time-series parameterization of the surface energy balance system (SEBS) over the qilian mountains. Remote Sens. (Basel) 7, 15822–15843.

Tuure, J., Mganga, K.Z., Mäkelä, P.S., Räsänen, M., Pellikka, P., Wachiye, S., Alakukku, L., 2025. Maize (Zea mays L.) yields and water productivity as affected by cowpea (Vigna unguiculata (L.) Walp.) Intercropping over five consecutive growing seasons in a semi-arid environment in Kenya. Agric. Water. Manage 319, 109779.

Vickers, D., Mahrt, L., 1997. Quality control and flux sampling problems for tower and aircraft data. J. Atmos. Ocean. Technol. 14, 512–526. https://doi.org/10.1175/1520-0426(1997)014<0512:QCAFSP>2.0.CO;2.

Vico, G., Porporato, A., 2011. From rainfed agriculture to stress-avoidance irrigation: I. A generalized irrigation scheme with stochastic soil moisture. Adv. Water. Resour. 34 (2), 263–271.

Volk, J., Huntington, J., Allen, R., Melton, F., Anderson, M., Kilic, A., 2021. Flux-data-qaqc: a python package for energy balance closure and post-processing of Eddy Flux data. J. Open. Source Softw. 6, 3418. https://doi.org/10.21105/joss.03418.

Wachiye, S., Merbold, L., Vesala, T., Rinne, J., Räsänen, M., Leitner, S., Pellikka, P., 2020. Soil greenhouse gas emissions under different land-use types in savanna ecosystems of Kenya. Biogeosciences 17, 2149–2167. https://doi.org/10.5194/bg-17-2149-2020.

Wanniarachchi, S., Sarukkalige, R., 2022. A review on evapotranspiration estimation in agricultural water management: past, present, and future. Hydrology 9, 123. https://doi.org/10.3390/hydrology9070123.

Webb, E.K., Pearman, G.I., Leuning, R., 1980. Correction of flux measurements for density effects due to heat and water vapour transfer. Quarterly J. Royal Meteorol. Soc. 106, 85–100. https://doi.org/10.1002/qj.49710644707.

Xu, J., Mu, Q., Ding, Y., Sun, S., Zou, Y., Yu, L., Zhang, P., Yang, N., Guo, W., Cai, H., 2023. Considering spatio-temporal dynamics of soil moisture with evapotranspiration partitioning helps to clarify water utilization characteristics of summer maize under deficit irrigation. J. Hydrol. 617, 129102.

Xue, J., Bali, K.M., Light, S., Hessels, T., Kisekka, I., 2020. Evaluation of remote sensing-based evapotranspiration models against surface renewal in almonds, tomatoes and maize. Agric. Water. Manage 238, 106228.

Yue, P., Zhang, Q., Ren, X., Yang, Z., Li, H., Yang, Y., 2022. Environmental and biophysical effects of evapotranspiration in semiarid grassland and maize cropland ecosystems over the summer monsoon transition zone of China. Agric. Water. Manage 264, 107462.

Zhang, X.F., Luo, C.L., Ren, H.X., Dai, R.Z., Mburu, D., Kavagi, L., Wesly, K., Nyende, A. B., Batool, A., Xiong, Y.C., 2020. Fully biodegradable film to boost rainfed maize (zea mays l.) production in semiarid kenya: an environmentally friendly perspective. Euro. J. Agronom. 119, 126124. https://doi.org/10.1016/j.eja.2020.126124.